Journal of Cluster Science (2023) 34:2521–2535
https://doi.org/10.1007/s10876-022-02400-9

ORIGINAL PAPER

Synergistic Effect of Iron and Copper Oxides in the Removal of Organic Dyes Through Thermal Induced Catalytic Degradation Process

Eman F. Aboelfetoh[1] · **Abdelmeguid E. Aboubaraka**[2] · **El-Zeiny M. Ebeid**[1]

Received: 2 September 2022 / Accepted: 1 December 2022 / Published online: 19 January 2023

Abstract

This study proposes a new method for producing α-Fe_2O_3–CuO nanocatalyst that is both cost-effective and ecologically benign. The α-Fe_2O_3–CuO nanocomposite was prepared via moderate thermal oxidative decomposition of copper hexacyanoferrate. Its structure and surface morphology are affirmed via XRD, SEM, FTIR, EDX, TEM, XPS, and VSM. In the presence of H_2O_2, α-Fe_2O_3–CuO is employed as a heterogeneous catalyst to stimulate thermally induced degradation of dyes such as direct violet 4, rhodamine b, and methylene blue. The synergistic effect of Fe_2O_3 and CuO enhanced the catalytic activity of the nanocomposite compared to Fe_2O_3 and CuO separately. The effectiveness of DV4 degradation is optimized by evaluating multiple reaction parameters. The reaction rate increased substantially with the temperature, revealing its key role in the degradation process. Higher H_2O_2 levels and the inclusion of inorganic anions like chloride or nitrate also sped up the degradation process. While sulfate and humic acid, particularly at high doses, slowed it. The mechanism of H_2O_2 activation on α-Fe_2O_3–CuO is studied. The measurements of chemical oxygen demand and total organic carbon indicate that all dyes are highly mineralized. The remarkable performance and stability of this nanocomposite in removing diverse dyes render it a promising option for wastewater remedy.

Keywords Copper hexacyanoferrate · Nanocomposite · α-Fe_2O_3–CuO · Oxidative decolorization · Kinetics

Introduction

Metal oxides have gained significant research attention owing to their chemical stability, catalytic, electrical and optical properties, and low cost [1, 2]. Because of their high density of surface sites and small size, metal oxide nanoparticles (NPs) have unique physical and chemical properties, compared to bulk materials [3]. Among the metal oxides NPs, cupric oxide (CuO), a p-type semiconductor material, exhibits remarkable electrical, optical, catalytic, adsorption, and biological properties [4, 5]. Since the morphologies of nanostructures have a strong influence on their efficiency, various CuO nanostructures have been synthesized using various methods namely, sol–gel, precipitation–pyrolysis, hydrothermal, solvothermal, microwave irradiation, and sonochemical methods [6, 7]. Another interesting metal oxide nanostructure is hematite (α-Fe_2O_3), which is an intriguing n-type semiconductor material, characterized by its chemical stability, natural abundance, nontoxicity, and low cost. Nanocomposites based on metal oxides have become increasingly popular in physics, chemistry, materials science, and engineering [8–10]. Various metal oxide nanocomposites such as CuO–ZnO, CeO_2–MnO_x, ZnO–MgO, ZnO–NiO, Co_3O_4–ZnO, and TiO_2–WO_3, have been fabricated and studied using various techniques. According to these studies, such nanocomposites have shown a higher photo-carrier separation performance than single oxides [8, 11]. They are mixtures of two or more different materials that combine the best qualities of the constituents to open new application opportunities, in which at least one material has nanoscale dimensions [10]. Numerous water treatment processes have used nanomaterials with special capabilities to remove diverse contaminants, including membrane separation, adsorption, coagulation, and others [12–15]. However, the primary objective of these techniques is to turn pollutants from an aqueous phase into a solid phase [16]. Advanced oxidation processes, or AOPs, are required

---

✉ Eman F. Aboelfetoh
eman.fahmy@science.tanta.edu.eg

[1] Chemistry Department, Faculty of Science, Tanta University, Tanta 31527, Egypt

[2] Central Lab of El-Gharbia Water and Wastewater Company, Tanta, Egypt

for the complete degradation of these contaminants and to prevent secondary contamination. Due to its effectiveness in destroying organic molecules, heterogeneous photocatalysis has emerged as one of the most intriguing AOPs [17–19]. There have been a lot of laboratory-scale studies on photocatalysis, but before it can be used in an industrial setting, there are some issues that need to be solved, including the lack of effective and affordable catalysts that can be used with a wider range of solar spectra instead of UV lamps and the design of reactors that are suitable for potential applications on a large scale [20]. In addition to photocatalysis, microwave-assisted catalysis has also been used to reduce pollutants, but it still has several disadvantages, such as high costs, energy consumption, and difficulties with large-scale use. The difficulty in scaling up microwave-induced processes is primarily caused by greater heat loss, changes in absorption, and a shallower radiation penetration depth into the reaction media [21].

One of the emerging applications of metal oxide nanocomposites is the degradation of organic dyes, which are considered one of the most hazardous substances detected in water supplies and wastewater. As mixed metal oxides, iron and copper oxides have recently gained significant attention for a variety of applications [22–24]. The combination of Fe_2O_3 and CuO into an Fe_2O_3–CuO nanocomposite achieves superior physical properties compared to Fe_2O_3 and CuO separately. This study thus presents a simple method for degrading various organic dyes in the absence of light, addressing the issue of insufficient light, using an α-Fe_2O_3–CuO nanocomposite synthesized via the low-temperature decomposition of readily available copper hexacyanoferrate ($Cu_2[Fe(CN)_6]$; CHCF). In the presence of hydrogen peroxide (H_2O_2), α-Fe_2O_3–CuO is used as a catalyst to activate the thermally induced degradation of direct violet 4 (DV4), methylene blue (MB) and rhodamine b (RhB) dyes. In the context of AOP technologies, this technique saves more energy than photocatalysis. Various experimental parameters are studied to assess their influence on the degradation efficiency of DV4. Meanwhile, the reactive species and mechanism of H_2O_2 activation by α-Fe_2O_3–CuO are investigated considering the experimental results.

Experimental

Materials

Potassium ferrocyanide, copper chloride dihydrate, H_2O_2, sodium hydroxide (NaOH), hydrochloric acid (HCl), sodium nitrate ($NaNO_3$), sodium chloride (NaCl) and sodium sulphate (Na_2SO_4) were obtained from Fluka. Humic acid was provided by Qualikems. Direct violet 4 (DV4), rhodamine B (RhB), and methylene blue (MB) were purchased from Acros and used without further purification (Scheme 1). Dilution and standard solutions were made with distilled water.

Synthesis of α-Fe_2O_3-CuO Nanocomposite

The α-Fe_2O_3–CuO nanocomposite was prepared via coprecipitation and low-temperature decomposition of the resulting complex (Scheme 2). Briefly, two aqueous solutions of potassium ferrocyanide (0.1 M) and copper chloride dihydrate (0.2 M) were prepared separately in 100 mL distilled water and then slowly mixed while stirring. Upon vigorous stirring for another 30 min, a dark brown precipitate was produced. The solid was collected, rinsed with distilled water several times, dried for 1 h at 90 °C, and further heated at 250 °C for 1 h to induce its decomposition. For comparative purposes, iron oxide was generated by combining the aqueous solutions of ferric chloride and potassium ferrocyanide, as previously reported [25]. The resulting complex (Prussian blue) was isolated, washed, and dehydrated at 90 °C for 1 h before heating at 250 °C for 1 h (Scheme 2). Meanwhile, cupric oxide (CuO) NPs are prepared through a precipitation process using NaOH as a precipitant. In a beaker of 50 mL distilled water, 0.2 M $CuCl_2·2H_2O$ was dissolved. Next, 0.5 M NaOH was introduced gradually while being agitated constantly until pH 10 was achieved. The resulting precipitate was washed, dried, and heated for 1 h at 250 °C.

Catalytic Activity of the α-Fe_2O_3-CuO Nanocomposite

In the presence of H_2O_2 (0.03 M), the α-Fe_2O_3–CuO nanocomposite (0.03 g) is introduced separately into 200 mL of $(1.4–10)\times10^{-5}$ M solutions of DV4, MB, and RhB dyes to assess its catalytic activity. The flasks containing the solutions are put in a water shaker thermostat (50 °C) for 30 min in the dark to reach equilibrium adsorption. After the catalyst is added to the reaction mixture, the kinetics measurements are initiated immediately.

A decrease in the absorbance of unreacted dye is immediately recorded using an ultraviolet–visible (UV–vis) spectrophotometer, and the measurements are performed until no further decline in absorption was observed. The efficiency of catalytic degradation was estimated using Eq. (1) as follows:

$$\mathbf{Degradation}(\%) = \frac{\mathbf{A_o - A_t}}{\mathbf{A_o}} \times 100 \quad (1)$$

where A_0 and A_t denote the absorbance of the dye before and after a specific period of the catalytic reaction, respectively.

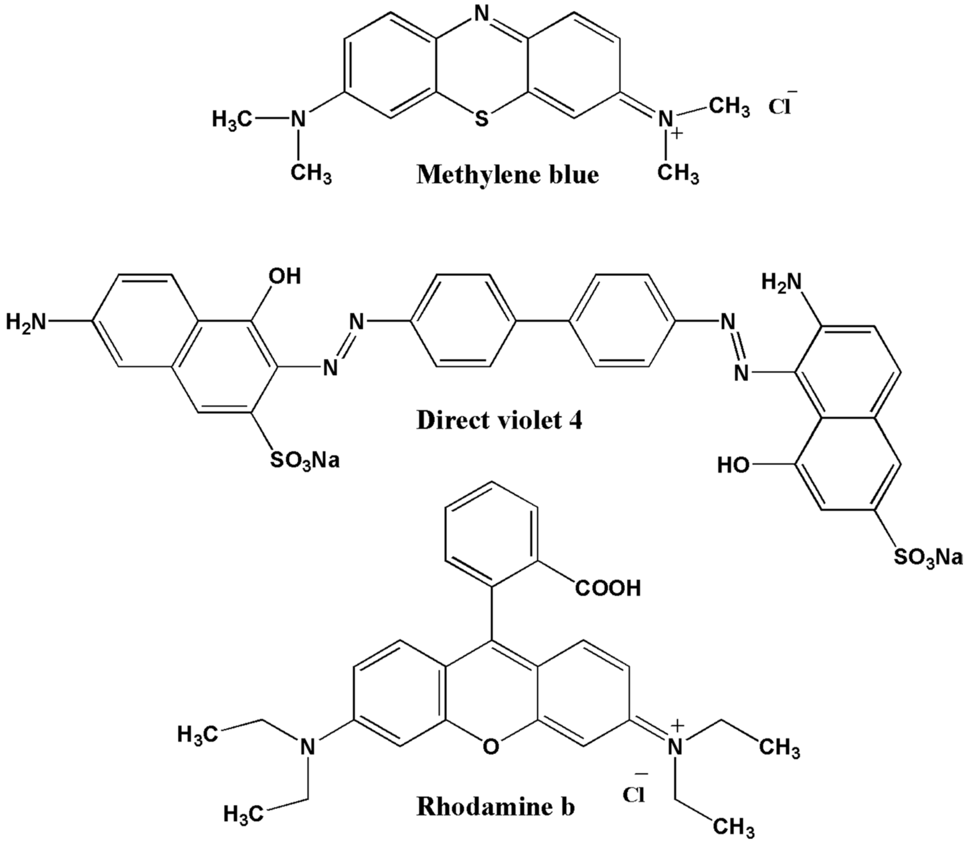

Scheme 1 Structure of organic dyes; methylene blue (MB), direct violet 4 (DV4), and rhodamine b (RhB)

Characterization

The XRD is used to characterize synthesized materials using a Rigaku MiniFlex 2 X-ray diffractometer. The FTIR spectra are obtained in a 4000–400 cm^{-1} range using a 670 (Nexus) Nicolet FTIR spectrophotometer in transmittance mode. A Cary Bio100 spectrophotometer is used to measure UV–vis spectra. SEM with EDX is used to analyze the nanocomposite's surface properties and composition (SEM–EDX; JEOL, JSM-IT100LA). Using TEM (JEOL, JSM-6360A), the particle size is identified. XPS was performed on K-ALPHA (Themo Fisher Scientific, USA) employing monochromatic X-ray Al K-α radiation "with a spot size of 400 µm, at pressure 10^{-9} mbar with full spectrum pass energy 200 eV and at narrow spectrum 50 eV".

The pH_{PZC}, or point of zero charge, of the nanocomposite, is identified as described previously [30]. In brief, several Erlenmeyer flasks were filled with 0.01 M NaCl solutions (50 mL). By adding HCl or NaOH solutions (0.1 M), the original pH was changed to 2, 4, 6, 8, 10, and 12. After that, each flask received 0.1 g of the nanocomposite, which was agitated for 24 h at room temperature. The pH_{PZC} is calculated by graphing the starting pH against the final pH of the solutions.

Results and Discussion

Characterization of the α-Fe_2O_3–CuO Nanocomposite

The surface morphology of the α-Fe_2O_3–CuO nanocomposite is investigated via SEM.

Figure 1a–c displays the corresponding micrographs, which clearly reveal the presence of two distinct structures (Fig. 1a). The presence of monoclinic particles indicates the formation of CuO NPs (Fig. 1b). Meanwhile, several nanorods corresponding to α-Fe_2O_3 can be also observed (Fig. 1c). The TEM image depicted in Fig. 1d confirms the nanosize of the synthesized α-Fe_2O_3–CuO nanocomposite, which exhibits a monoclinic crystalline structure of CuO NPs with highly dispersed α-Fe_2O_3 nanorods on the surface. Figure 2 illustrates the XRD patterns of the synthesized materials. As previously mentioned, the heating of Prussian blue at 250 °C resulted in an amorphous phase of Fe_2O_3 (Fig. 2 inset) [25]. The peaks at $2\theta = 17.64°$, 25.04°, 35.79°, 40.1°, 44.0°, 51.4°, 55.0°, and 57.8° in the complex pattern (Fig. 2a) are indicative of the cubic crystalline structure of the CHCF complex [26]. Figure 2b exhibits the distinctive peaks of the monoclinic phase of CuO NPs at 2θ values of 35.60°, 39.14°, 49.22°, and 58.35° which correspond well with the standard JCPDS no. 45–0937. The XRD pattern

Scheme 2 Preparation of the α-Fe_2O_3-CuO nanocomposite

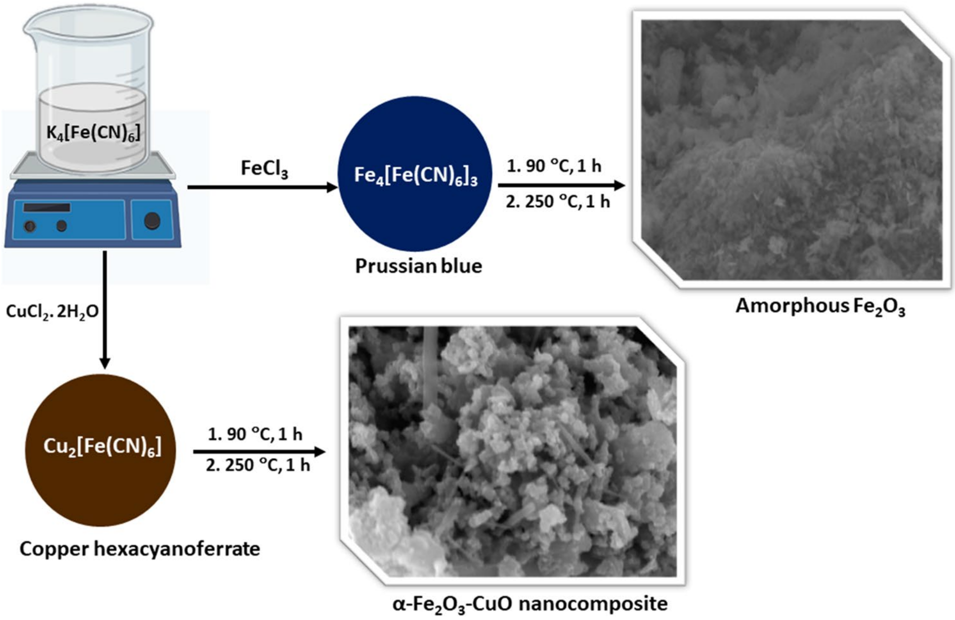

obtained for the α-Fe_2O_3–CuO composite (Fig. 2c) displays the characteristic peaks of a high density CuO phase, albeit slightly shifted, and small diffractions of α-Fe_2O_3 at 2θ values of 24.20°, 33.07°, 35.98°, 40.75°, 49.40°, 53.90°, and 57.40°, indicating the successful synthesis of the composite α-Fe_2O_3–CuO structure. According to the Debye–Scherrer formula [27], the average crystalline size of the CuO/α-Fe_2O_3 nanocomposite is determined to be 14 nm. The FTIR spectra of the CHCF complex, the α-Fe_2O_3–CuO nanocomposite, amorphous Fe_2O_3, and CuO NPs are shown in Fig. 3.

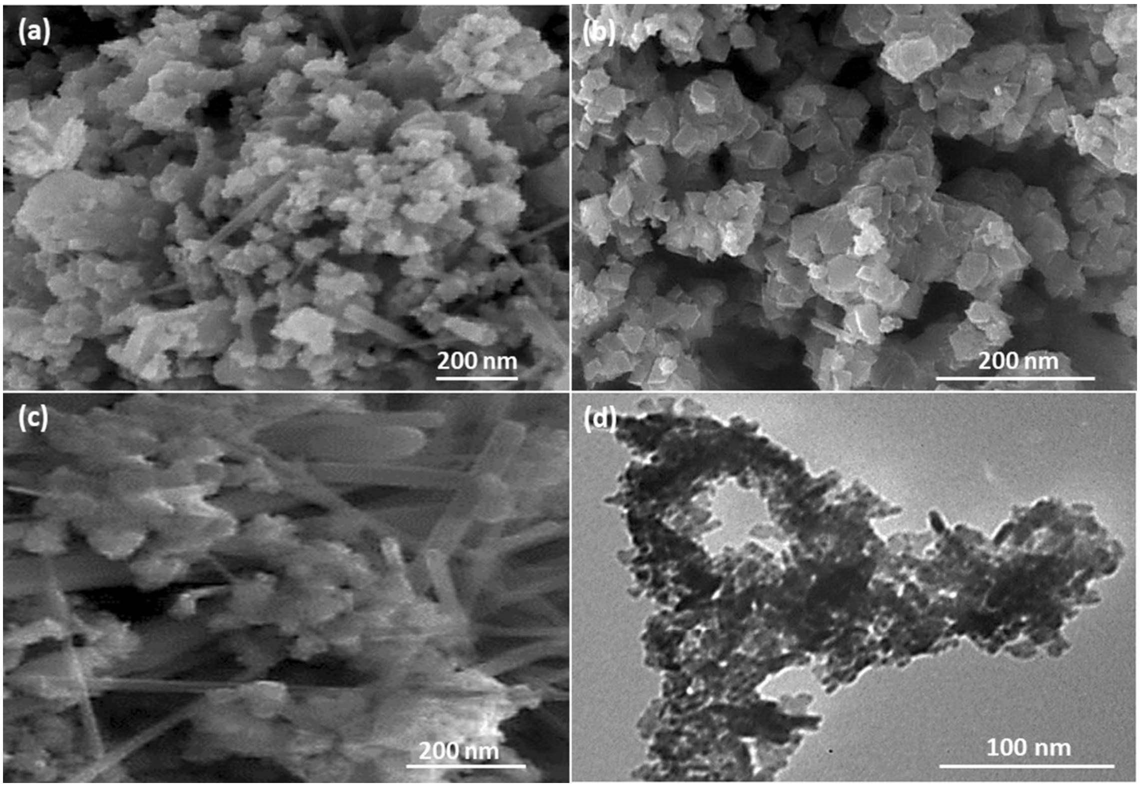

Fig. 1 SEM (**a–c**) and TEM (**d**) images of the α-Fe_2O_3–CuO nanocomposite

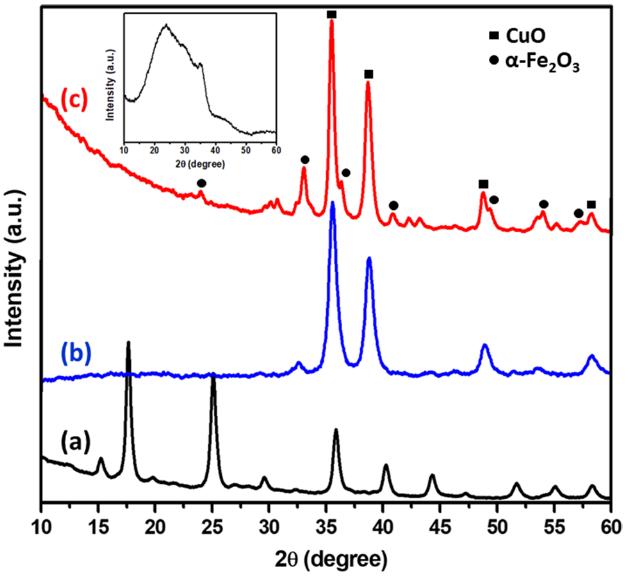

Fig. 2 XRD patterns of the synthesized materials; CHCF complex (a), CuO NPs (b), and α-Fe_2O_3-CuO nanocomposite (c), and the inset refers to amorphous Fe_2O_3

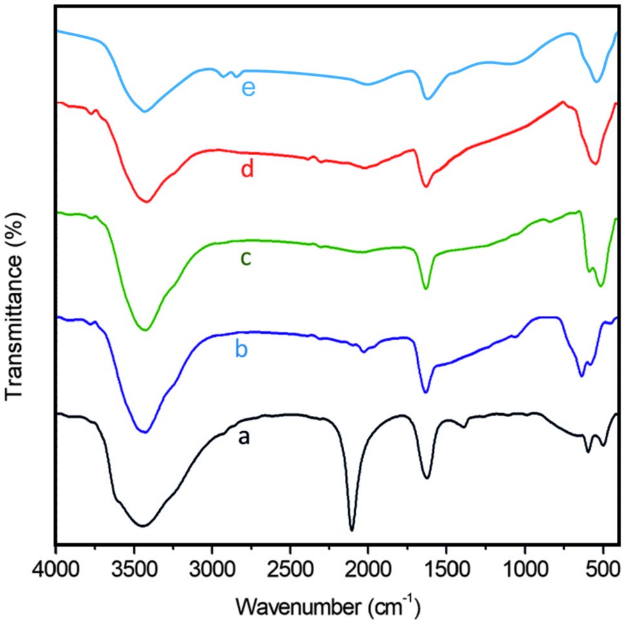

Fig. 3 FTIR spectra of the synthesized materials; (a) CHCF complex, (b) amorphous Fe_2O_3, (c) CuO NPs, (d) and (e) α-Fe_2O_3–CuO nanocomposite before and after the catalytic reaction

The spectrum of the CHCF complex exhibits a broad band at 3434 cm^{-1} and another band at 1630 cm^{-1} due to the O–H groups stretching and bending vibrations indicating the presence of water. A high intensity band at 2107 cm^{-1} is associated with the stretching vibration of cyanide group of the Fe^{II}–CN–Cu^{II} bonds, confirming the presence of Fe(II) in the compound structure [26, 28]. Additional bands at 595 and 500 cm^{-1} might be attributable to the Fe–C and Cu–N stretching vibrations, respectively [28]. In the spectrum of Fe_2O_3, besides the characteristic bands of OH groups, two bands appear at around 575 and 631 cm^{-1} corresponding to Fe–O stretching. The spectrum of CuO NPs shows bands in the range of 498–580 cm^{-1} attributable to Cu–O vibrations, confirming the formation of CuO NPs [29]. Meanwhile, the spectrum of the α-Fe_2O_3–CuO nanocomposite features a band at 544 cm^{-1} corresponding to the overlap of Cu–O and Fe–O bands, which is in accord with the formation of a composite between α-Fe_2O_3 and CuO. EDX spectroscopy is used to identify the elemental composition and the percentage of each element within the substance. Figure 4 shows the EDX distribution of the synthesized nanocomposite, which reveals the presence of Cu, Fe, and O as elementary components in α-Fe_2O_3–CuO. The weight percentages of Fe, Cu, and O in the synthesized sample were 21%, 49%, and 30%, respectively, suggesting that the Fe to Cu ratio is 1:2. The magnetic property of the synthesized sample was examined using a vibrating sample magnetometer, VSM. The saturation magnetization (*Ms*) of α-Fe_2O_3–CuO is 4.90 emu g^{-1}, as outlined in Fig. 5a. This reflects the nearly superparamagnetic nature of the nanocomposite. The α-Fe_2O_3–CuO was swiftly extracted from the reaction solution using an external magnet. The optical band gap (E_g) is related to the absorption coefficient (α) and photon energy (hυ) by the Tauc equation $\alpha h\upsilon = A\ (h\upsilon - E_g)^n$, where A is a constant, and n is an index that varies depending on the mechanism of interband transitions, with $n = 2$ or 1/2 referring to indirect or direct transitions, respectively [30]. The E_g value of α-Fe_2O_3-CuO is obtained from the intersection of the extrapolation of the linear part of the curve (Fig. 5b). The best linear match was obtained by plotting $(\alpha h\upsilon)^2$ against hυ, and the direct E_g value of nanocomposite is determined to be 2.92 eV. This value is higher than that of bulk CuO; in addition, the band

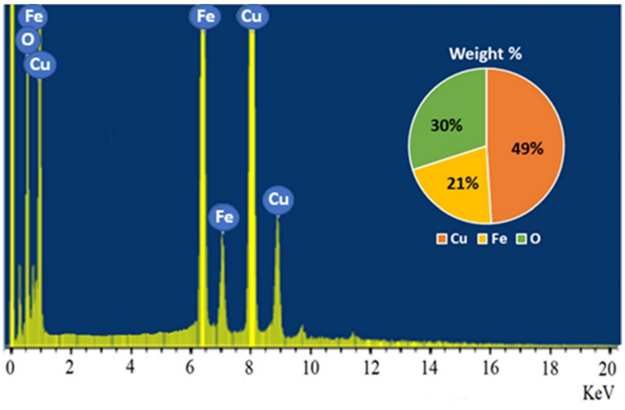

Fig. 4 EDX of the α-Fe_2O_3–CuO nanocomposite

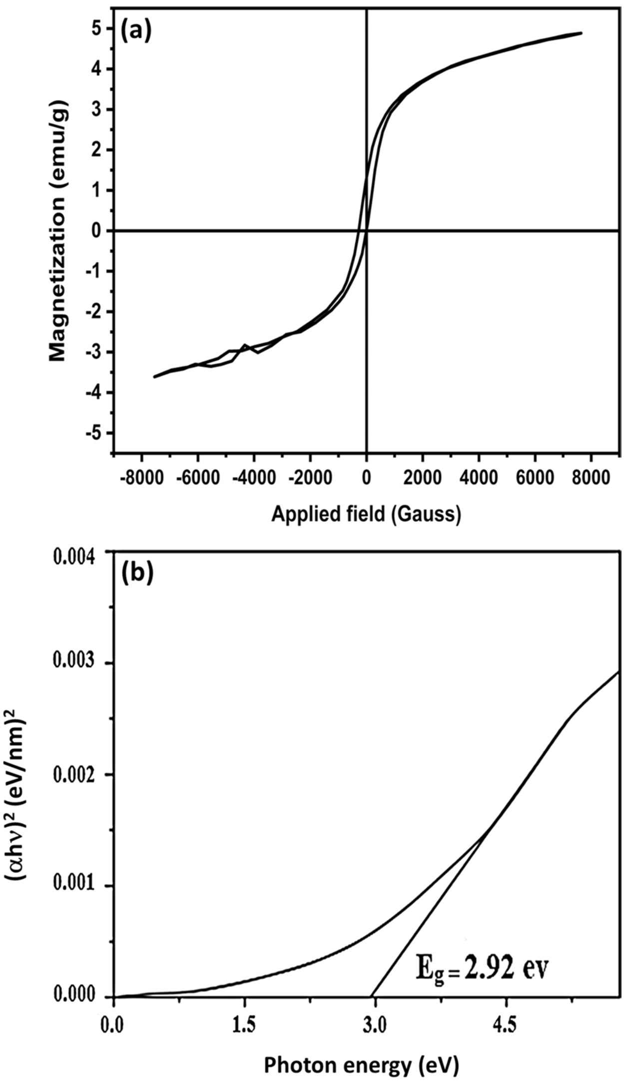

Fig. 5 Magnetization curve (**a**), and Tauc plot (**b**) of the α-Fe_2O_3–CuO nanocomposite

gap energy increases as the particle size decreases due to quantum confinement effects [31].

The α-Fe_2O_3–CuO nanocomposite's composition and oxidation state are determined using XPS analysis. The XPS survey of α-Fe_2O_3–CuO reflects the existence of O 1 s (57.97%), Cu 2p3 (25.72%), and Fe 2p (14.15%), as seen in Fig. 6a. The Fe 2p3/2 and Fe 2p1/2 of Fe^{3+} species are indicated by two peaks in Fig. 6b, which are situated at 710.5 and 723.9 eV, respectively [32, 33]. The satellite peak at 717.7 eV is typical of Fe^{3+} in α-Fe_2O_3 [34]. The high-resolution spectrum for Cu was depicted in Fig. 6c, and the peaks at 953.5 and 933.27 eV, is attributed to Cu $2p_{1/2}$ and Cu $2p_{3/2}$ of Cu^{2+}, respectively [30, 35]. This confirms the presence of CuO in the nanocomposite. CuO is also supported by the existence of the shake-up peaks (satellites) at 961.7, 943.4, and 941.0 eV, which are situated at higher binding energies to the main peaks and suggest the existence of an unfilled shell (Cu $3d^9$) of Cu^{2+} [30]. The main peak for the O 1 s XPS spectrum in Fig. 6d denotes the lattice oxygen of Fe–O and Cu–O with a binding energy of 529.9 eV. The other peak is located around 531.5 eV and represents the surface OH species [34, 36].

Degradation Kinetic Study

Organic dyes are common compounds that are widely used in many fields. As a result, massive amounts of dyes are released into streaming waste. AOPs have gained increasing attention in textile and dye wastewater treatment. In this study, to assess the catalytic deterioration efficiency of α-Fe_2O_3–CuO, DV4, MB, and RhB are selected as model dye contaminants in aqueous media because of their toxicity and resistance to degradation. The degradation tests were performed with H_2O_2 as an ecofriendly oxidant. The activation of H_2O_2 to create an efficient oxidizing species still constitutes a challenge. When a catalyst is added, oxygen reactive species, primarily OH radicals, are generated as the primary oxidizing species. In the absence of a catalyst, the mixture (dye/H_2O_2) remained stable for several hours with no change in absorbance, indicating that no reaction occurred between the dyes and H_2O_2. The decrease in absorbance caused by the catalytic degradation of DV4, RhB and MB in the presence of H_2O_2 is depicted in Fig. 7. The catalytic reaction kinetics followed a pseudo-first-order model (Eq. 2), where the initial H_2O_2 concentration was at least 150 times higher than the dye concentration:

$$\mathbf{\ln(A_0/A_t) = k_{obs}t} \tag{2}$$

where K_{obs} (min^{-1}) denotes the observed rate constant and t (min) denotes the dye removal time.

Effect of Operating Factors on Azo Dye DV4 Degradation

Figure 8a shows a comparison between the nanocomposite's catalytic activity and that of amorphous Fe_2O_3 and CuO NPs, as well as the mechanical mixing of CuO and Fe_2O_3 with a 2 to 1 ratio, as in the nanocomposite. The synthesized α-Fe_2O_3–CuO nanocomposite displayed the highest DV4 degradation efficiency. This result reveals that the synergistic interaction of Fe_2O_3 and CuO significantly enriched the catalytic active sites and improved the DV4 degradation efficiency. Numerous variables, including catalyst dose, dye concentration, temperature, contact time, and reaction pH may have an impact on the catalytic activity of α-Fe_2O_3–CuO. To optimize the catalytic process, the variables having the highest impact must be identified.

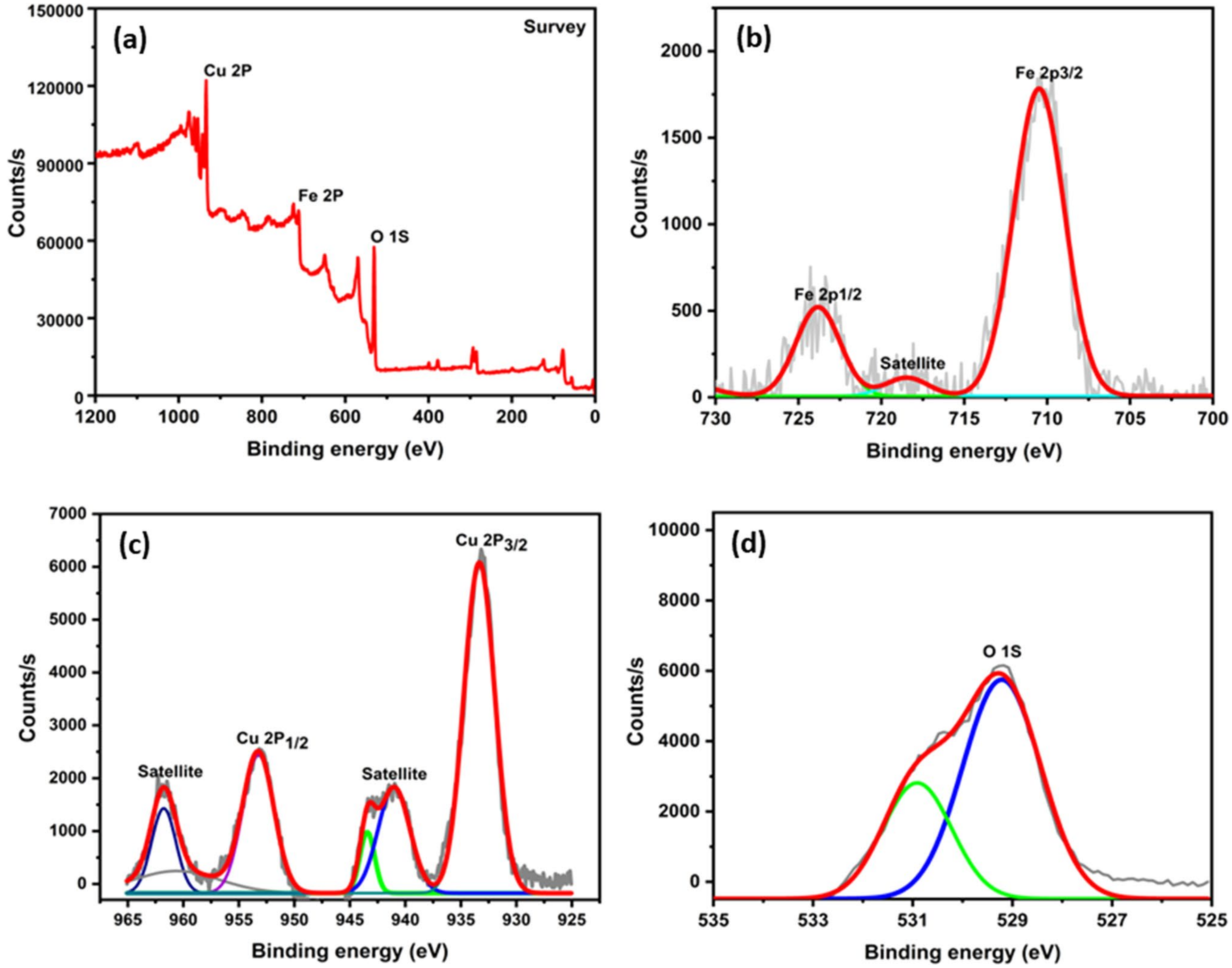

Fig. 6 XPS survey (**a**) and high-resolution spectra of the Fe 2p (**b**), Cu 2p (**c**), and O 1 s (**d**) of the nanocomposite

Effect of the H_2O_2 Concentration A series of blank experiments revealed that H_2O_2 has no effect on the DV4 degradation in the absence of the catalyst and about 20% of the dye is degraded within 1 h in the presence of α-Fe_2O_3–CuO alone. When H_2O_2 was added to the reaction media, the percentage of dye degradation notably increased. The effect of the H_2O_2 concentration (0.01–0.07 M) on the degradation efficiency of DV4 (4×10^{-5} M) is investigated using a constant dose of catalyst (0.03 g) at 50 °C and pH 6. Figure 8b, c shows the degradation efficiency over time and first-order graphs for the oxidative reaction of DV4 at varied H_2O_2 concentrations. The percentage and rate constant values of the dye degradation (Table 1) increased with the H_2O_2 concentration. This could be due to the production of hydroxyl radicals ($HO^{\bullet}$), which attack DV4 molecules. The generation of highly active $HO^{\bullet}$ has been previously connected with the activation of H_2O_2 by heterogeneous catalysts [37].

Effect of the Catalyst Dose The effect of catalyst dose on the DV4 (4×10^{-5} M) degradation efficiency is investigated by changing the amount of α-Fe_2O_3–CuO from 0.01 to 0.06 g at 50 °C, while maintaining the H_2O_2 concentration at 0.03 M. The obtained results are shown in Fig. 9a and Table 1. The degradation efficiency and rate constant increased as the catalyst dose is increased to 0.04 g. This tendency could be explained by the existence of more active sites, which leads to the production of more reactive radicals ($HO^{\cdot}$). Upon further increasing the catalyst dose beyond the optimum level, the deterioration rate decreased, which could be due to the self-quenching of a large number of radicals produced by H_2O_2 instead of the reaction with dye molecules. The formation of aggregates between catalyst particles, which would decrease the number of available sites for the activation of H_2O_2, might be another reason behind the decrease in the degradation rate at a high catalyst dose.

Fig. 7 Absorption spectra of direct violet 4 (DV4; 7×10^{-5}) (**a**), ▶ methylene blue (MB; 3×10^{-5}) (**b**), and rhodamine b (RhB; 2×10^{-5}) (**c**) recorded at different time intervals in the presence of 0.03 g of α-Fe_2O_3–CuO nanocomposite and H_2O_2 (0.03 M) at 50 °C

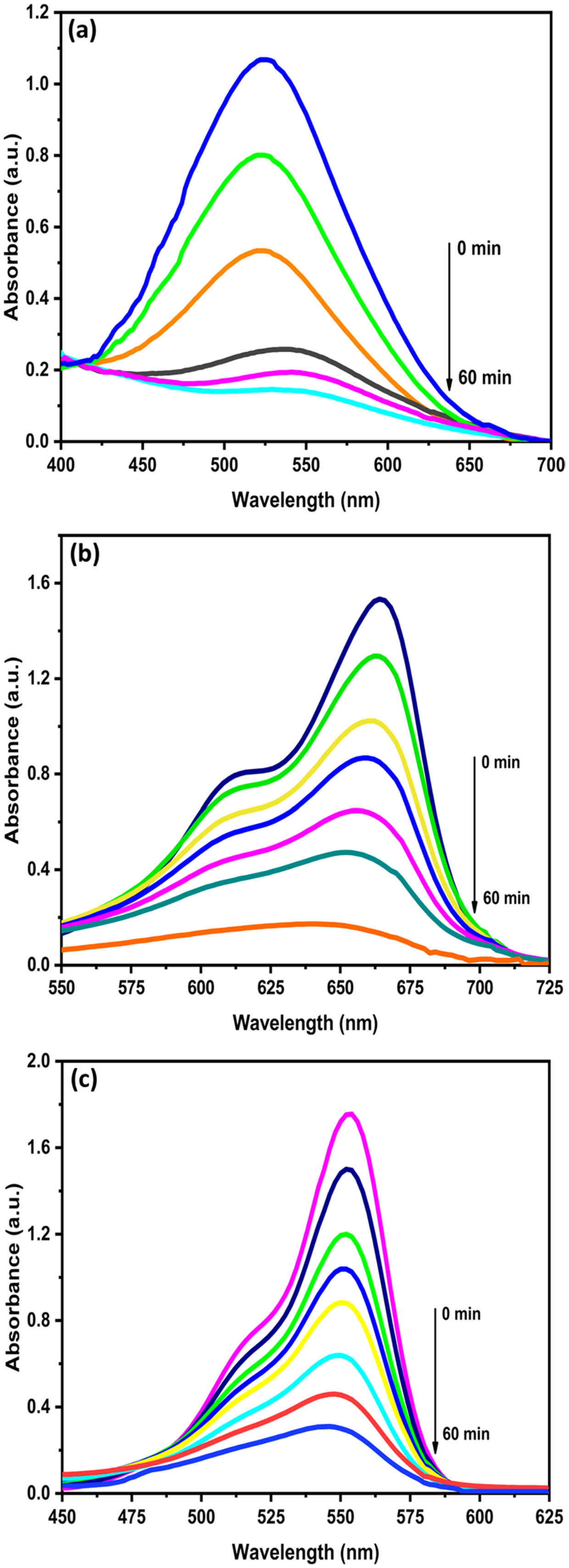

Effect of the DV4 Concentration The effect of varying the initial DV4 concentration from 1.4×10^{-5} to 10×10^{-5} M was studied, while the H_2O_2 concentration and the catalyst dose were kept constant at 0.03 M and 0.03 g, respectively (Fig. 9b). At a low DV4 concentration (1.4×10^{-5} M), the degradation percentage reached almost 100% within 15 min; however, it declined upon further increasing the DV4 concentration. As can be seen in Table 1, raising the DV4 concentration resulted in a drop in the rate constant. This drop is attributable to excessive DV4 molecules covering the catalyst's active sites.

Effect of Temperature In most oxidation processes, temperature is a critical parameter, especially in industrial and environmental applications. The temperature effect on the reaction rate is analyzed at 25, 37, 50, and 70 °C, while H_2O_2 (0.03 M), the concentration of DV4 (4×10^{-5} M), and the catalyst dose (0.03 g) were kept constant. The degradation efficiency increased dramatically upon increasing the reaction temperature. Thus, increasing the temperature from 25 to 70 °C resulted in a degradation efficiency of 87% within 2 min (Fig. 9c) and an increase in the reaction rate from 0.057 to 0.894 min^{-1} (Table 1). The considerable increase in the degradation efficiency at high temperature is attributable to the production of additional radicals, which contribute to the oxidation of DV4 molecules into reaction products. According to prior studies, heat speeds up the reaction and produces more active radicals [38, 39]. The activation energy (E_a) is calculated from the Arrhenius plot (not shown). Furthermore, thermodynamic parameters $\Delta G^\#$, $\Delta S^\#$, and $\Delta H^\#$ are determined from the Eyring and Gibbs equations and are listed in Table 2. The catalytic process was endothermic, as indicated by the positive enthalpy value. The E_a value was in the common range of chemical reactions.

Effect of pH The solution pH is a significant parameter that affects the oxidative degradation of organic pollutants. The efficiency of the catalyst in the degradation of DV4, RhB and MB was investigated at the pH levels of 4, 6, 8, and 10. As depicted in Fig. 10a, the highest degradation percentage (100%) for DV4 is obtained at a pH of 6. However, the degradation efficiency decreased upon further increasing the pH. This is because the surface properties of the catalyst are influenced by pH changes. The pH_{PZC} of α-Fe_2O_3–CuO is estimated to be 7.8 following the reported method [10]. At $pH < pH_{PZC}$ (7.8), the catalyst's surface becomes positively charged, whereas at $pH > pH_{PZC}$, it becomes negatively

Fig. 8 Degradation percentage of DV4 over time using 0.03 g of different catalysts and 0.03 M H_2O_2 (**a**), degradation percentage of DV4 over time (**b**), and the first-order plots (**c**) using 0.03 g of α-Fe_2O_3–CuO in the presence of diverse concentrations of H_2O_2 at 50 °C

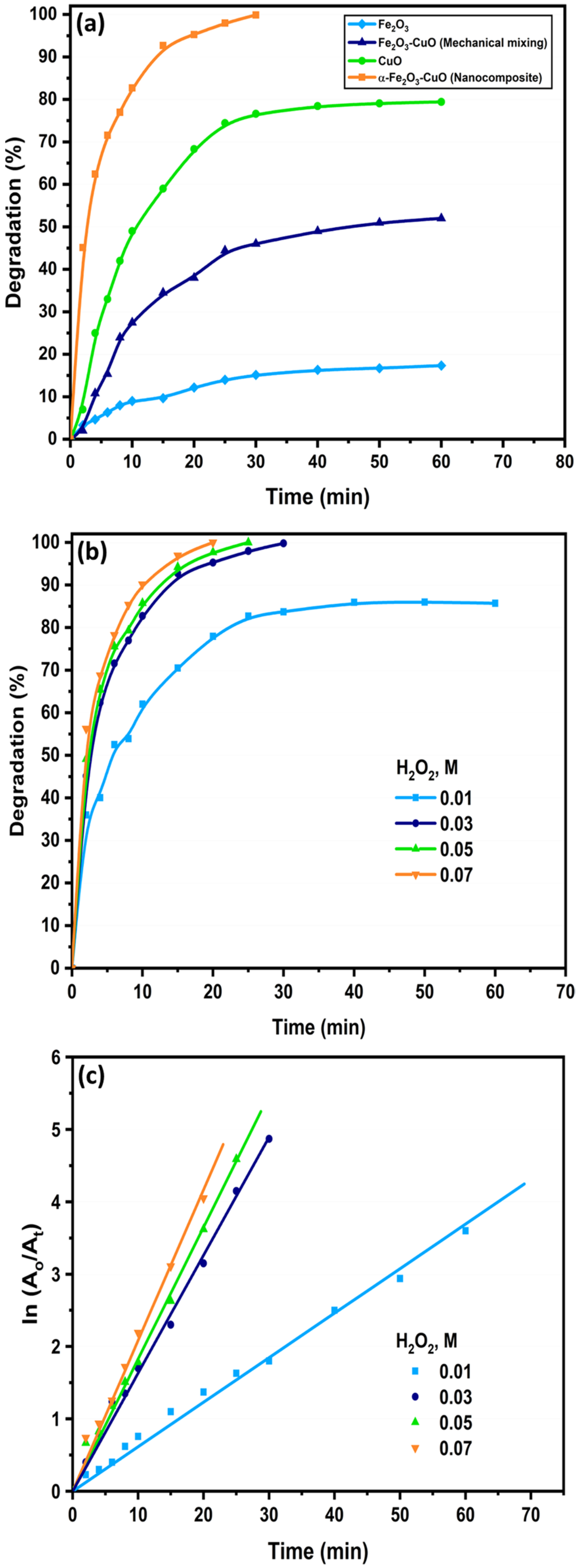

charged. DV4 is an anionic dye, and at pH 6, the catalyst surface owns a positive charge that attracts the DV4 dye molecules more strongly, increasing the degradation rate. For RhB, the maximum degradation (95.3%) is achieved at pH 4. At this pH, the positively charged catalyst surface attracts RhB molecules, which is a zwitterionic structure in a polar solvent [40]. The formation of the zwitterion is favored as the pH increases, which contributes to the RhB aggregation and formation of dimers [40]. Therefore, the degradation efficiency of the catalyst diminishes at higher pH values. In contrast, the MB degradation increased efficiency upon increasing the pH value from 4 to 10. MB is a cationic dye, and at $pH > pH_{PZC}$ the catalyst surface becomes negatively charged which attracts the MB molecules more strongly, resulting in an enhancement of the degradation rate.

Effect of Ultraviolet Irradiation Generally, the combination of ultraviolet (UV) light irradiation and H_2O_2 results in a complete degradation of organic dyes. During the oxidation process, highly oxidative species such as $HO^{\bullet}$ are formed. In the present study, an aqueous solution of DV4 (4×10^{-5} M) remained relatively stable upon UV irradiation in the absence of H_2O_2 or the catalyst (not shown). In contrast, when the reaction mixture (DV4, catalyst, and H_2O_2) is exposed to UV light (254 nm), the degradation rate constant increased dramatically from 0.163 to 0.54 min^{-1}, as seen in Fig. 10b. This enhancement reveals that UV irradiation produces high concentrations of free radical species.

Effect of Inorganic Ions In natural and wastewater, various inorganic anions including chloride (Cl^-), nitrate (NO_3^-), and sulfate (SO_4^{2-}) are frequently found [41]. So, it is essential to investigate how they affect the degradation rate of DV4 dye. The effects of added SO_4^{2-}, Cl^-, and NO_3^- ions on the degradation rate are investigated separately at constant doses of the α-Fe_2O_3–CuO catalyst and DV4 with various quantities of Na_2SO_4, NaCl, and $NaNO_3$. The degradation rate of DV4 is decreased by the SO_4^{2-} ion concentration, as seen in Fig. 11a. The thermally induced catalytic activity in the presence of SO_4^{2-} ions appears to produce $SO_4^{\bullet-}$ radicals, according to eqs. 3 and 4.[42] The $^{\bullet}OH$ radicals or holes are captured by the SO_4^{2-} anions, which prevents deterioration. The excess SO_4^{2-} decelerated the degradation rate of DV4 because the generated $SO_4^{\bullet-}$ is less reactive than $^{\bullet}OH$ and h^+ [42].

$$\mathbf{SO_4^{2-} + h^+ \rightarrow SO_4^{\bullet-}} \tag{3}$$

Table 1 Catalytic degradation of direct violet 4 (DV4) by nanocatalyst (α-Fe_2O_3-CuO) under different conditions after 1 h

Catalytic reaction conditions	Varied parameters	K_{obs} (min^{-1})	R^2	Degradation %
[DV4] = 4×10^{-5} M, catalyst dose (0.03 g), 50 °C, and pH = 6	$[H_2O_2]$/M			
	0.01	0.061	0.998	85.7
	0.03	0.163	0.996	100
	0.05	0.174	0.997	100
	0.07	0.191	0.998	100
[DV4] = 4×10^{-5} M, $[H_2O_2]$ = 0.03 M 50 °C, and pH = 6	Catalyst dose g^{-1}			
	0.01	0.059	0.987	85.03
	0.02	0.081	0.995	93.84
	0.03	0.163	0.996	100
	0.04	0.271	0.994	100
	0.06	0.180	0.998	100
$[H_2O_2]$ = 0.03 M, catalyst dose (0.03 g), 50 °C, and pH = 6	[DV4] × 10^{-5}/M			
	1.4	0.180	0.994	100
	4	0.163	0.996	100
	7	0.084	0.985	95
	10	0.062	0.977	86
[DV4] = 4×10^{-5}, $[H_2O_2]$ = 0.03 M, catalyst dose (0.03 g), and pH = 6	Temperature °C			
	25	0.057	0.982	82.1
	37	0.079	0.988	93.03
	50	0.163	0.996	100
	70	0.894	0.997	100
[DV4] = 4×10^{-5}, $[H_2O_2]$ = 0.03 M, catalyst dose (0.03 g), and 50 °C	pH			
	4	0.140	0.969	98.8
	6	0.163	0.996	100
	8	0.130	0.983	97.1
	10	0.083	0.987	92

$$\mathbf{SO_4^{2-} + {}^{\bullet}OH \rightarrow SO_4^{\bullet-} + OH^-} \tag{4}$$

By contrast, the rate of DV4 degradation rises with increasing NaCl concentration (Fig. 11b). This is primarily caused by an increase in reactive chlorine species (RCS: $Cl^{\bullet}$, $Cl_2^{\bullet-}$, $ClOH^{\bullet-}$, etc.), which hastened the degradation rate of DV4. Earlier studies reported a similar outcome [41, 43]. Like Cl^-, rising NO_3^- ion concentrations accelerate the rate of deterioration (Fig. 11c). This considerable boost in performance is attributed to the production of more reactive species ($^{\bullet}OH$ and $NO_2^{\bullet}$) because of NO_3 photolysis [41, 44].

Effect of Humic Acid Natural organic matters, or NOMs, are a group of carbon-based substances that are found in a variety of groundwater resources and surface waters. Humic substances make up a sizable component of NOMs [45]. So, the impact of various humic acid, HA, concentrations on the rate of DV4 degradation is assessed (Fig. 12). At a low dose of HA (1–5 mg L^{-1}), the DV4 degradation was ≥ 98%, as depicted in Fig. 12a. At 1 and 5 mg L^{-1} HA, the rate constants reduced marginally from 0.163 min^{-1} to 0.162 and 0.158 min^{-1}, respectively (Fig. 12b). With increasing HA dose to 10, 20, and 35 mg L^{-1}, the degradation rates decreased to 0.136, 0.115, and 0.088 min^{-1}, respectively. This can be attributed to HA's capacity to operate as a radical scavenger of $^{\bullet}OH$ as well as the radical competition between HA and DV4 molecules [33, 46].

Dyes Mineralization

The purpose of the catalytic degradation process is not only the decolorization of the dye but also its mineralization, that is, its decomposition into CO_2 and H_2O. The dye decolorization was measured using a UV–vis spectrophotometer. The dye absorption bands for DV4, MB, and RhB disappeared entirely, indicating that the dyes were rapidly degraded, and the aromatic system was fully destroyed. The total organic carbon (TOC) analysis technique was used to measure the total quantity of carbon in organic compounds converted to CO_2 during an oxidation reaction. The TOC removal percentage is about 91% following 2 h of catalytic degradation

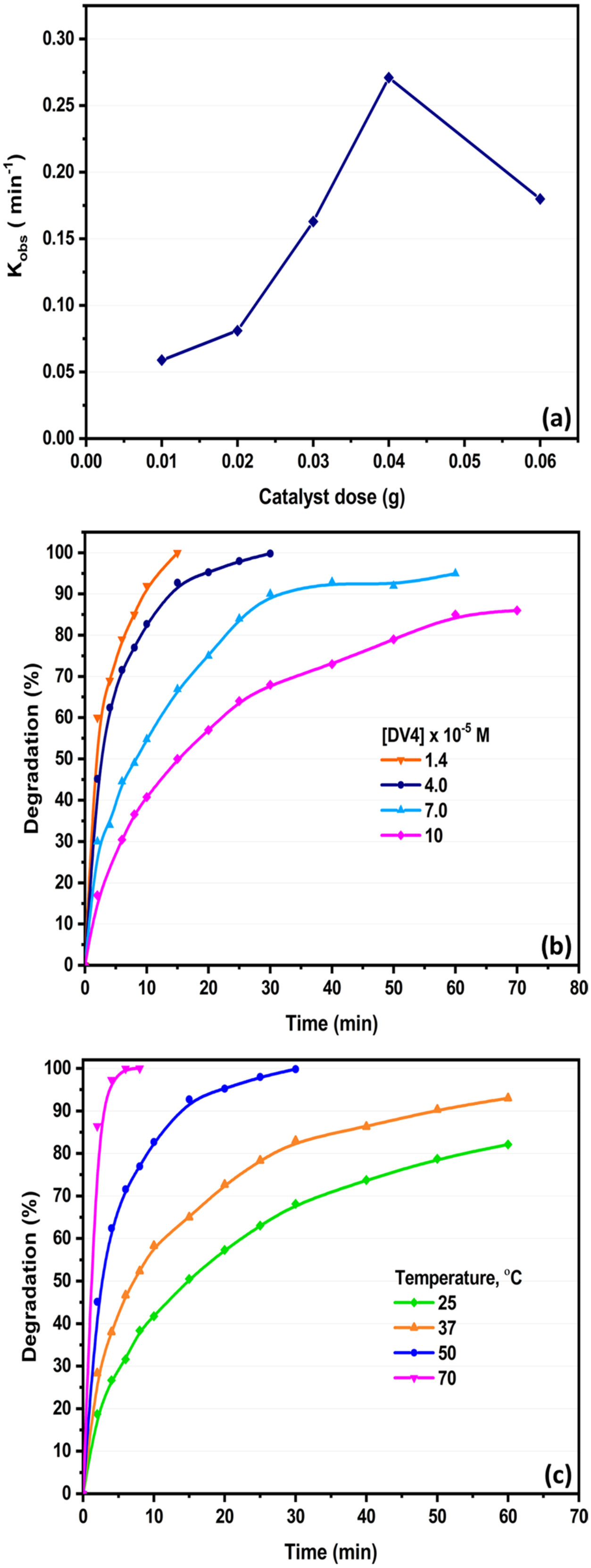

Fig. 9 The rate constant as a function of catalyst dose (**a**), degradation percentage of DV4 over time in the presence of 0.03 g of α-Fe_2O_3-CuO nanocomposite at various DV4 concentrations (**b**) and at various reaction temperatures (**c**)

Table 2 The activation parameters and observed rate constant values of the catalytic degradation of direct violet 4 (DV4) using nanocatalyst (0.03 g), and H_2O_2 (0.03 M), at different temperatures

Temperature (°C)	K (min^{-1})	E (kJ mol^{-1})	$\Delta H^{\#}$ (kJ mol^{-1})	$\Delta G^{\#}$ (kJ mol^{-1})	$\Delta S^{\#}$ (J mol^{-1} K)
25	0.057	52.58	49.93	83.35	− 103.48
37	0.079				
50	0.163				
70	0.894				

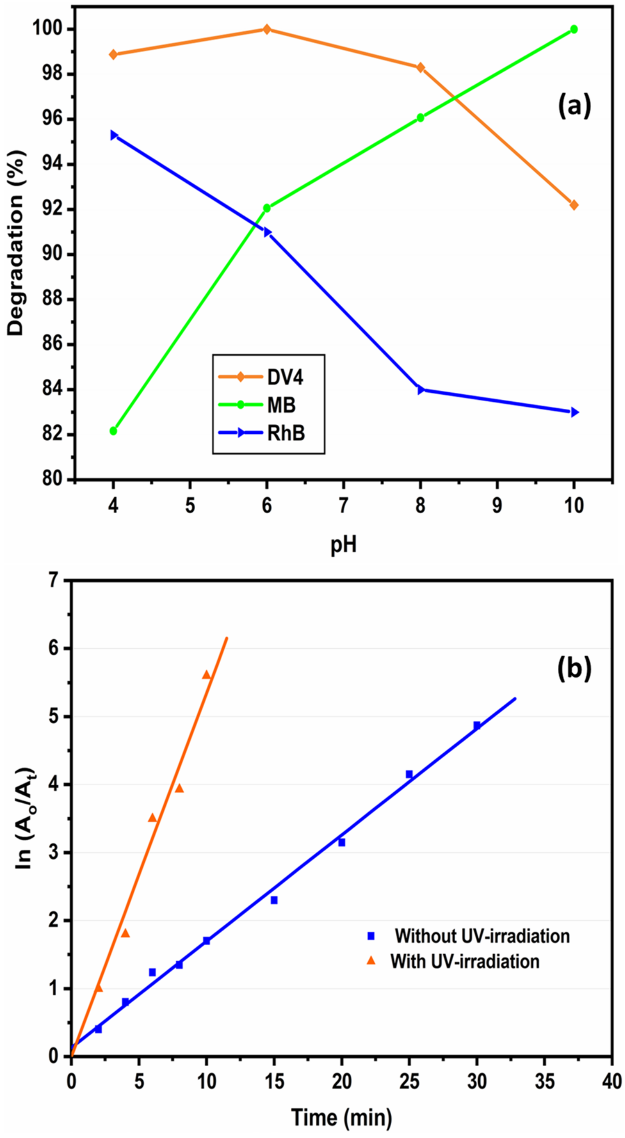

Fig. 10 Degradation percentage of DV4, MB, and RhB at various pH values (**a**), and the effect of ultraviolet irradiation (**b**) on the degradation of DV4 (4×10^{-5}) using 0.03 g of α-Fe_2O_3-CuO nanocomposite and H_2O_2 (0.03 M) at pH 6 and 50 °C

Fig. 11 Degradation rate constants of DV4 (4×10^{-5} M) using 0.03 g ▶ of α-Fe_2O_3-CuO and 0.03 M H_2O_2 in the presence of various concentrations of **a** Na_2SO_4, **b** NaCl, and **c** $NaNO_3$ at 50 °C

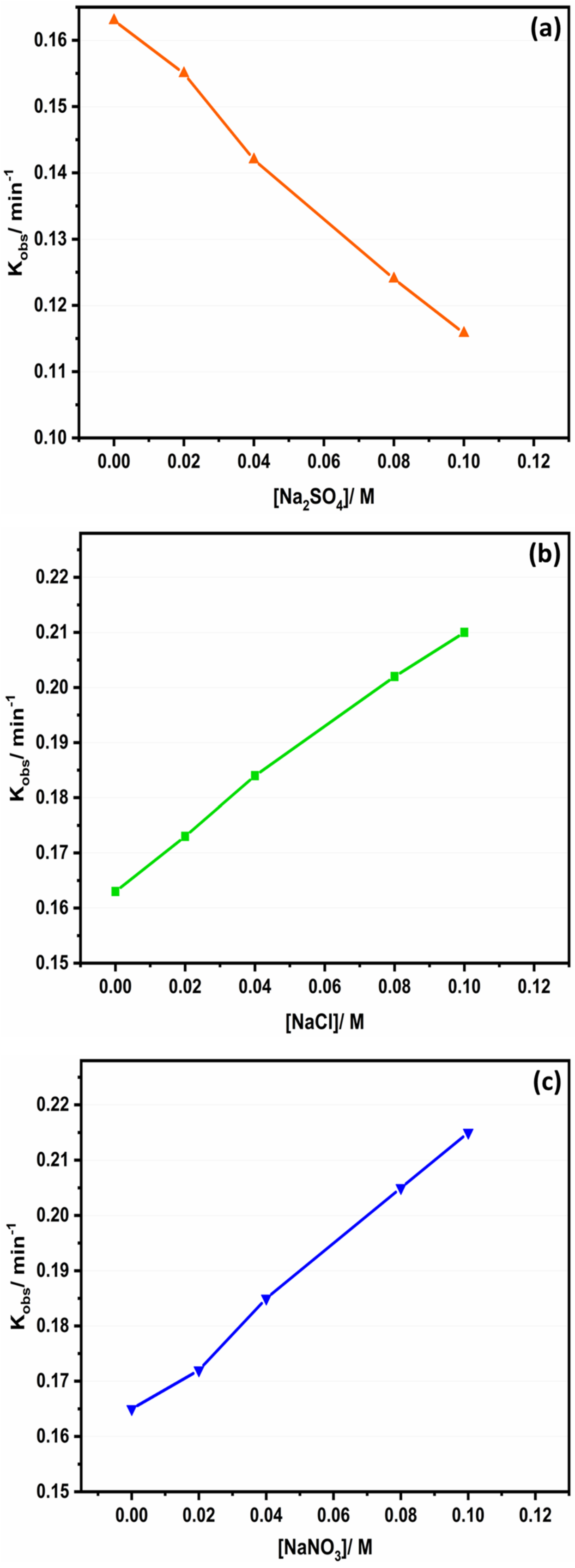

of DV4 (4×10^{-5} M) in the presence of H_2O_2 at pH 6 and 50 °C. The reduction in TOC is due to ring-opening mechanisms, which convert the aromatic molecules to aliphatic ones. For MB, the catalyst reached a 90% TOC removal, whereas a TOC removal of 81% is obtained in the case of RhB. These experiments are performed at the optimum pH values for the degradation of MB and RhB. Moreover, the chemical oxygen demand (COD) is measured by using a powerful oxidizing agent to completely oxidize any organics into CO_2 under acidic conditions. After the catalytic degradation process, the COD removal percentage for DV4, MB, and RhB were 95%, 93%, and 85%, respectively. The observed reduction of COD demonstrates that the starting organic dyes were oxidized to mineral ions.

Degradation Mechanism

To investigate the mechanism of the α-Fe_2O_3–CuO nanocatalyst in the oxidative degradation of DV4 dye, studies were conducted to trap reactive species during the thermo-induced catalytic reaction. The selected scavengers are tert-butyl alcohol (TBA, $^{\bullet}OH$ radical scavenger), benzoquinone (BQ, $O_2^{\bullet}$ scavenger), and disodium ethylenediaminetetraacetic acid (EDTA, h^+ scavenger). They were added individually to a 100 mL reaction solution at a concentration of 0.4 M. In the absence of a scavenger, the degradation rate constant of DV4 was 0.163 min^{-1}. As shown in Fig. 13a, adding BQ to the DV4 solution decreased the rate of degradation slightly (0.147 min^{-1}), whereas the addition of EDTA resulted in a significant reduction in the degradation rate (0.003 min^{-1}). When TBA was used, the degradation rate of DV4 dropped from 0.163 to 0.070 min^{-1}. These findings suggest that $^{\bullet}OH$ and h^+ are responsible for DV4 dye's degradation.

One of the most effective strategies that have been considered to improve photocatalytic performance is the formation of a heterojunction between numerous semiconductors [47–50]. In the current study, a possible degradation mechanism is suggested in the schematic design of Fig. 13b based on the active species trapping results. A p-n heterojunction will form at the interface of the synthesized α-Fe_2O_3-CuO nanocomposite because α-Fe_2O_3 (n-type) and CuO (p-type) have differing band gaps and electronegativity [50–52]. As a result, an internal electric field is formed at the interface [51, 52]. Under the circumstances of thermal activation, the excited electrons from the valence bands (VB) of α-Fe_2O_3 and CuO migrate to the corresponding conduction bands (CB) [38]. CuO's high CB position and the interface's internal electric field cause electrons to move from CuO to α-Fe_2O_3 and holes to move the other way [50].

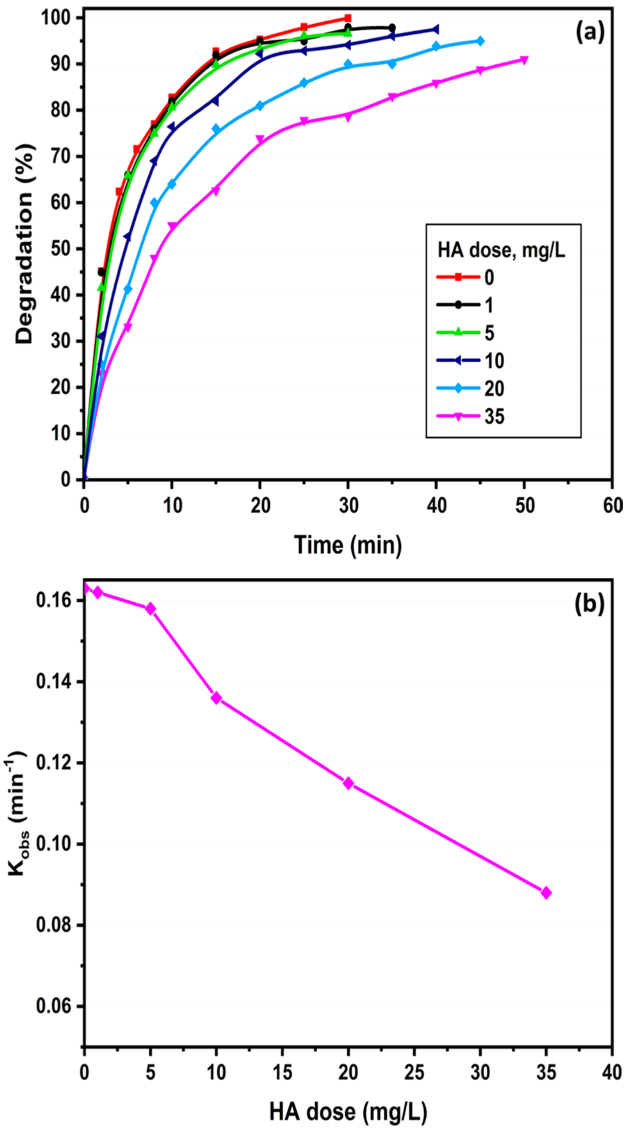

Fig. 12 Degradation percentage (**a**) and rate constants (**b**) of DV4 (4×10^{-5} M) using 0.03 g of α-Fe_2O_3-CuO and 0.03 M H_2O_2 in the presence of diverse doses of humic acid at 50 °C

Thus, a successful partition of electrons and holes happens at the interface. Furthermore, according to the double charge transfer mechanism the electrons will be accumulated in the conduction band of α-Fe_2O_3 and the holes will be accumulated in the valence band of CuO [50, 53]. When α-Fe_2O_3–CuO is present alone, the catalytic degradation efficacy is limited because of electron and hole recombination. With the addition of H_2O_2, the results demonstrate a rapid rate of degradation (Fig. 8b, c). Where H_2O_2 inhibits the recombination of free carriers by trapping electrons. H_2O_2 molecules are then reduced and converted to OH^- and $^{\cdot}OH$. Furthermore, $^{\cdot}OH$ can be produced by trapping holes in the valence band with surface-bound H_2O or OH^- (adsorbed and free) [54].

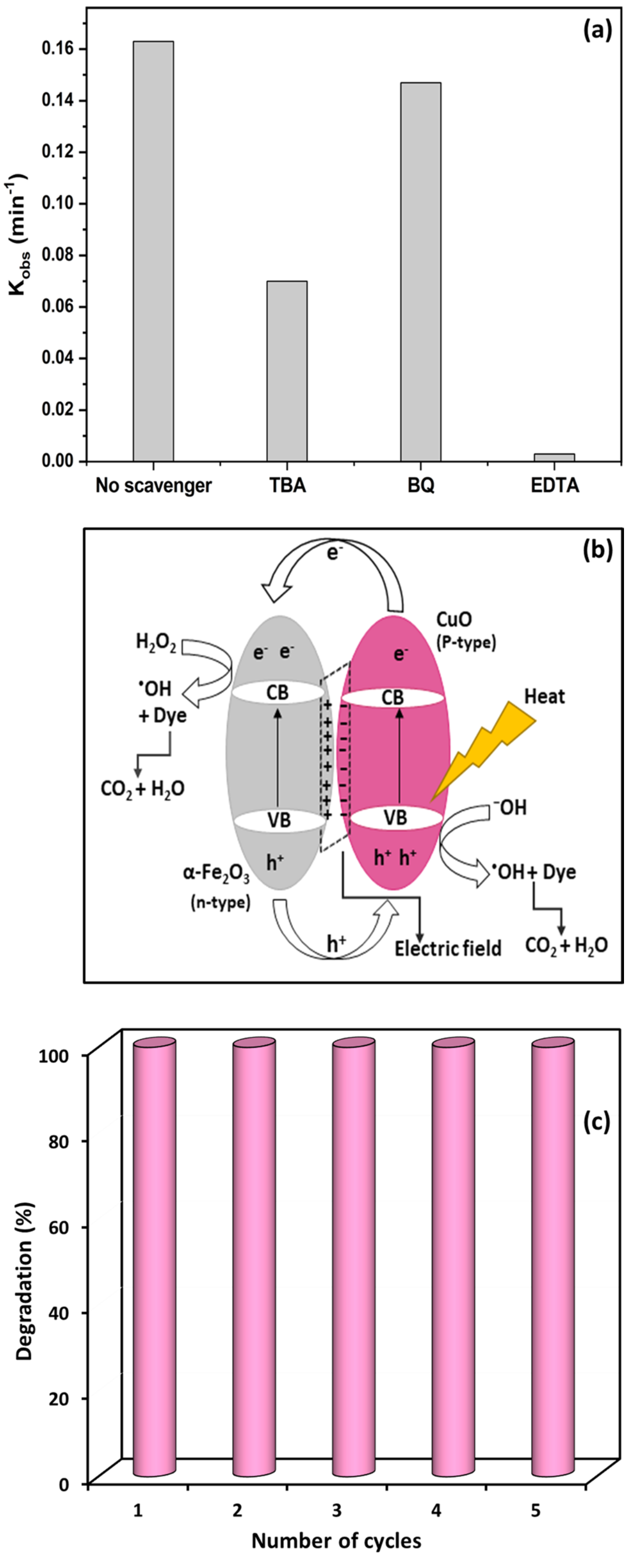

Fig. 13 The effect of different scavengers (**a**) on the degradation of DV4 (4×10^{-5}) using 0.03 g of α-Fe_2O_3-CuO nanocomposite and H_2O_2 (0.03 M) at pH 6 and 50 °C, proposed illustration of the thermally induced catalytic degradation of DV4 dye by a p–n heterojunction (**b**) and the effect of nanocatalyst recycling on the DV4 degradation percentage (**c**)

Therefore, the thermally generated positive hole (h^+) in (VB) and an electron (e^-) in (CB) are considered powerful oxidizing and reductive agents respectively and the oxidation/reduction reactions can be represented by the following Eqs. (5–9):

$$\mathbf{\alpha - Fe_2O_3 - CuO + thermal\,excitation \rightarrow e^-(CB) + h^+(VB)} \tag{5}$$

$$\mathbf{H_2O_2 + e^- \rightarrow {}^{\bullet}OH + OH^-} \tag{6}$$

$$\mathbf{H_2O + h^+ \rightarrow {}^{\bullet}OH + H^+} \tag{7}$$

$$\mathbf{h^+ + OH^- \rightarrow {}^{\bullet}OH} \tag{8}$$

$$\mathbf{Dye + {}^{\bullet}OH \rightarrow CO_2 + H_2O} \tag{9}$$

Catalyst Reuse

The catalyst's reusability is a crucial factor in determining how cost-effective the process is. Therefore, the recovery and recyclability of the α-Fe_2O_3–CuO catalyst were examined in the oxidation of DV4 with H_2O_2. The catalyst can be regenerated in a straightforward manner. Using an external magnet, the catalyst was magnetically recovered from the media after two hours of disintegration. It was thoroughly washed with distilled water, dried (at 60 °C for 12 h), and then used once more in the reaction's subsequent cycle. Figure 13c depicts the degradation efficiency of DV4 as a function of cycle number. The results reveal that the DV4 degradation percentage remained constant at approximately 100% throughout five cycles. The nanocomposite's FTIR spectrum is assessed following three regeneration cycles to investigate its stability. The spectrum revealed the distinctive bands of the α-Fe_2O_3–CuO nanocomposite, as illustrated in Fig. 3. Moreover, ICP/OES (inductively coupled plasma-optical emission spectrometry) analysis showed that almost no Cu or Fe leached from the catalyst surface into the solution proving the stability of the catalyst. The nanocomposite (α-Fe_2O_3–CuO) is therefore an appropriate option for the remediation of dye-contaminated water.

Conclusion

This study provides an ecofriendly and cost-effective technique for the synthesis of an α-Fe_2O_3–CuO nanocomposite. The α-Fe_2O_3–CuO nanocomposite is successfully prepared via oxidative conversion of CHCF in air at a low decomposition temperature. Techniques like XRD, SEM, EDX, FTIR, XPS, VSM, and TEM described the α-Fe_2O_3–CuO nanocomposite. It showed excellent activity for the degradation of DV4, MB, and RhB in the presence of H_2O_2 with the aid of temperature (≥ 50 °C). During thermal activation, the electrons on the VB are transferred to the CB because a higher temperature can promote the charge transfer of electrons and holes at semiconductors. Meanwhile, the rest of the electrons on the CB are trapped and oxidized by H_2O_2 to produce $^{\bullet}$OH. The released radicals and the existing free holes oxidize the organic dyes. The degradation rate of the dye is influenced by the H_2O_2 concentration as well as the catalyst dose. Inorganic anions (Cl^-, NO_3^-, and SO_4^{2-}) and humic acid, especially at high doses, have a notable impact on the degradation as well. According to pH impact, RhB and DV4 are more favored in acid media, whereas MB degradation proceeded better in alkaline media. TOC and COD measurements revealed that a significant portion of DV4, MB, and RhB dyes are degraded to CO_2, H_2O, and some inorganic acids. Moreover, the catalyst showed excellent recyclability after five runs. The α-Fe_2O_3–CuO nanocomposite's capacity to degrade the three dyes and its reusability make it an effective catalyst for treating wastewater.

Funding Open access funding provided by The Science, Technology & Innovation Funding Authority (STDF) in cooperation with The Egyptian Knowledge Bank (EKB).

Declarations

Conflict of interest The authors declare that they have no conflict of interest.

References

1. E. F. Aboelfetoh, M. Fechtelkord, and R. Pietschnig (2010). *J. Mol. Catal. A: Chem.* **318**, 51–59.
2. E. F. Aboelfetoh and R. Pietschnig (2014). *Catal. Lett.* **144**, 97–103.
3. A. M. Radwan, E. F. Aboelfetoh, T. Kimura, T. M. Mohamed, and M. M. El-Keiy (2021). *Biomed. Res. Ther.* **8**, 4483–4496.
4. Y.-K. Phang, M. Aminuzzaman, M. Akhtaruzzaman, G. Muhammad, S. Ogawa, A. Watanabe, and L.-H. Tey (2021). *Sustainability* **13**, 796.
5. E. F. Aboelfetoh, A. A. Elhelaly, and A. H. Gemeay (2018). *J. Environ. Chem. Eng.* **6**, 623–634.

6. A. Klinbumrung, T. Thongtem, and S. Thongtem (2014). *Appl. Surf. Sci.* **313**, 640–646.
7. E. Alp, H. Eşgin, M. K. Kazmanlı, and A. Genc (2019). *Ceram. Int.* **45**, 9174–9178.
8. A. O. Juma, E. A. Arbab, C. M. Muiva, L. M. Lepodise, and G. T. Mola (2017). *J. Alloys Compd.* **723**, 866–872.
9. A. H. Gemeay, R. G. Elsharkawy, and E. F. Aboelfetoh (2018). *J. Polym. Environ.* **26**, 655–669.
10. E. F. Aboelfetoh, M. E. Z. Elabedien, and E.-Z.M. Ebeid (2021). *J. Environ. Chem. Eng.* **9**.
11. R. K. Sharma, D. Kumar, and R. Ghose (2016). *Ceram. Int.* **42**, 4090–4098.
12. S. Yu, H. Tang, D. Zhang, S. Wang, M. Qiu, G. Song, D. Fu, B. Hu, and X. Wang (2022). *Sci. Total Environ.* **811**.
13. E. F. Aboelfetoh, A. E. Aboubaraka, and E.-Z.M. Ebeid (2021). *J. Environ. Manage.* **288**.
14. E. F. Aboelfetoh, A. H. Gemeay, and R. G. El-Sharkawy (2020). *Environ. Monit. Assess.* **192**, 1–20.
15. A. E. Aboubaraka, E. F. Aboelfetoh, and E.-Z.M. Ebeid (2017). *Chemosphere* **181**, 738–746.
16. B. Abebe, H. Murthy, and E. Amare (2018). *J. Encapsulation Adsorpt. Sci.* **8**, 225–255.
17. M. Hao, M. Qiu, H. Yang, B. Hu, and X. Wang (2021). *Sci. Total Environ.* **760**.
18. L. Yao, H. Yang, Z. Chen, M. Qiu, B. Hu, and X. Wang (2021). *Chemosphere* **273**.
19. X. Liu, R. Ma, L. Zhuang, B. Hu, J. Chen, X. Liu, and X. Wang (2021). *Crit. Rev. Environ. Sci. Technol.* **51**, 751–790.
20. M. Umar and H. A. Aziz, Photocatalytic degradation of organic pollutants in water, in M. N. Rashed (ed.), *Organic Pollutants—Monitoring, Risk and Treatment* (InTech, London, 2013), pp. 195–208.
21. A. De La Hoz, J. Alcázar, J. Carrillo, M. A. Herrero, J. D. M. Muñoz, P. Prieto, A. De Cózar, and A. Diaz-Ortiz, Reproducibility and Scalability of Microwave-Assisted Reactions, in U. Chandra (ed.), *Microwave Heating* (InTech, Croatia, 2011), pp. 137–162.
22. Y.-F. Zhao, Z.-Y. Yang, Y.-X. Zhang, L. Jing, X. Guo, Z. Ke, P. Hu, G. Wang, Y.-M. Yan, and K.-N. Sun (2014). *J. Phys. Chem. C* **118**, 14238–14245.
23. P. Li, H. Jing, J. Xu, C. Wu, H. Peng, J. Lu, and F. Lu (2014). *Nanoscale* **6**, 11380–11386.
24. Q. Tian, W. Wu, L. Sun, S. Yang, M. Lei, J. Zhou, Y. Liu, X. Xiao, F. Ren, and C. Jiang (2014). *ACS Appl. Mater. Interfaces* **6**, 13088–13097.
25. R. Zboril, L. Machala, M. Mashlan, and V. Sharma (2004). *Cryst. Growth Des.* **4**, 1317–1325.
26. S. Xiang, X. Zhang, Q. Tao, and Y. Dai (2019). *J. Radioanal. Nucl. Chem.* **320**, 609–619.
27. C. Chen, B. Yu, J. Liu, Q. Dai, and Y. Zhu (2007). *Mater. Lett.* **61**, 2961–2964.
28. R. Martins, D. Martins, L. Costa, T. Matencio, R. Paniago, and L. Montoro (2020). Int. J. 418 Hydrog. *Energy* **45**, 25708–25718.
29. R. Zaidi, S.U. Khan, A. Azam, I.H. Farooqi (2021). IOP Conf. Ser.: Mater. Sci. Eng. **1058**, 012074.
30. E. C. Pastrana, V. Zamora, D. Wang, and H. Alarcón (2019). *Adv. Nat. Sci.-Nanosci. Nanotechnol.* **10**.
31. A. K. Bhunia and S. Saha (2020). *BioNanoScience* **10**, 89–105.
32. K. Al-Namshah (2021). *Appl. Nanosci.* **11**, 467–476.
33. Y. Yang, W. Ji, X. Li, H. Lin, H. Chen, F. Bi, Z. Zheng, J. Xu, and X. Zhang (2022). *J. Hazard. Mater.* **424**.
34. C. Ye, K. Hu, Z. Niu, Y. Lu, L. Zhang, and K. Yan (2019). *J. Water Process. Eng.* **27**, 205–210.
35. Y. Wang, N. Lin, Y. Gong, R. Wang, and X. Zhang (2021). *Chemosphere* **280**.
36. Y. Yang, S. Zhao, F. Bi, J. Chen, Y. Li, L. Cui, J. Xu, and X. Zhang (2022). *Cell Rep. Phys. Sci.* **3**.
37. N. T. Thao, H. T. P. Nga, N. Q. Vo, and H. D. K. Nguyen (2017). *J. Sci.: Adv. Mater. Devices* **2**, 317–325.
38. C. Zhou, X. Sun, J. Yan, B. Chen, P. Li, H. Wang, J. Liu, X. Dong, and F. Xi (2017). *Powder Technol.* **308**, 114–122.
39. Y.-Y. Lau, Y.-S. Wong, T.-Z. Ang, S.-A. Ong, N. A. Lutpi, and L.-N. Ho (2018). *Environ. Sci. Pollut. Res.* **25**, 7067–7075.
40. S. D. Khairnar and V. S. Shrivastava (2019). *J. Taibah Univ. Sci.* **13**, 1108–1118.
41. X. Ding, L. Gutierrez, J.-P. Croue, M. Li, L. Wang, and Y. Wang (2020). *Chemosphere* **253**.
42. F. T. Joorabi, M. Kamali, and S. Sheibani (2022). *Mater. Sci. Semicond. Process.* **139**.
43. N. T. Hoang, V. T. Nguyen, N. D. M. Tuan, T. D. Manh, P.-C. Le, D. Van Tac, and F. M. Mwazighe (2022). *Chemosphere* **298**.
44. Y. Wu, L. Bu, X. Duan, S. Zhu, M. Kong, N. Zhu, and S. Zhou (2020). *J. Clean Prod.* **273**.
45. M. T. Ghaneian, P. Morovati, M. H. Ehrampoush, and M. Tabatabaee (2014). *J. Environ. Health Sci. Eng.* **12**, 1–7.
46. R. Zhuan and J. Wang (2020). *Sep. Purif. Technol.* **234**.
47. Y. Li, M. Wu, Y. Wang, Q. Yang, X. Li, B. Zhang, and D. Yang (2020). *Front. Chem.* **8**, 75.
48. Y. Zou, Y. Hu, Z. Shen, L. Yao, D. Tang, S. Zhang, S. Wang, B. Hu, G. Zhao, and X. Wang (2022). *J. Environ. Sci.* **115**, 190–214.
49. M. Fang, X. Tan, Z. Liu, B. Hu, X. Wang (2021). Research, **2021**, 19 p.
50. M. Pirhashemi, A. Habibi-Yangjeh, and S. R. Pouran (2018). *J. Ind. Eng. Chem.* **62**, 1–25.
51. S. K. Lakhera, A. Watts, H. Y. Hafeez, and B. Neppolian (2018). *Catal. Today* **300**, 58–70.
52. J. Low, J. Yu, M. Jaroniec, S. Wageh, and A. A. Al-Ghamdi (2017). *Adv. Mater.* **29**, 1601694.
53. M. Qiu, B. Hu, Z. Chen, H. Yang, L. Zhuang, and X. Wang (2021). *Biochar* **3**, 117–123.
54. B. Abramović, V. Despotović, D. Šojić, and N. Finčur (2015). *React. Kinet. Mech. Catal.* **115**, 67–79.